

Gross Discrepancies between Observed and Simulated Twentieth-to-Twenty-First-Century Precipitation Trends in Southeastern South America

ARIANNA M. VARUOLO-CLARKE,^{a,b} JASON E. SMERDON,^a A. PARK WILLIAMS,^{a,c} AND RICHARD SEAGER^a

^a *Lamont-Doherty Earth Observatory, Columbia University, Palisades, New York*

^b *Department of Earth and Environmental Sciences, Columbia University, New York, New York*

^c *Department of Geography, University of California, Los Angeles, Los Angeles, California*

(Manuscript received 23 September 2020, in final form 16 March 2021)

ABSTRACT: Southeastern South America (SESA; encompassing Paraguay, southern Brazil, Uruguay, and northern Argentina) experienced a 27% increase in austral summer precipitation from 1902 to 2019, one of the largest observed trends in seasonal precipitation globally. Previous research identifies Atlantic multidecadal variability and anthropogenic forcing from stratospheric ozone depletion and greenhouse gas emissions as key factors contributing to the positive precipitation trends in SESA. We analyze multimodel ensemble simulations from phases 5 and 6 of the Coupled Model Intercomparison Project (CMIP) and find that not only do Earth system models simulate positive SESA precipitation trends that are much weaker over the historical interval, but some models persistently simulate negative SESA precipitation trends under historical forcings. Similarly, 16-member ensembles from two atmospheric models forced with observed historical sea surface temperatures never simulate precipitation trends that even reach the lower bound of the observed trend's range of uncertainty. Moreover, while future twenty-first-century projections from CMIP6 yield positive ensemble mean precipitation trends over SESA that grow with increasing greenhouse gas emissions, the mean forced response never exceeds the observed historical trend. Preindustrial control runs from CMIP6 indicate that some models do occasionally simulate centennial-scale trends in SESA that fall within the observational range, but most models do not. Results point to significant uncertainties in the attribution of anthropogenically forced influences on the observed increases in precipitation over SESA while also suggesting that internal decadal-to-centennial variability of unknown origin and not present in state-of-the-art models may have also played a large role in generating the twentieth-to-twenty-first-century SESA precipitation trend.

KEYWORDS: Precipitation; Climate variability; Climate models; Model comparison


1. Introduction

Southeastern South America (SESA) encompasses the area east of the Andes Mountains ($\sim 64^\circ\text{W}$) between 20° and 40°S , including southern Brazil, Paraguay, Uruguay, and northern Argentina, and experiences significant precipitation variability on interannual to decadal time scales. This variability has serious implications for agriculture, river flow, water resources, and power generation in SESA (Robertson and Mechoso 1998; Viglizzo and Frank 2006; Seager et al. 2010). Co-occurring with this decadal-to-multidecadal variability, SESA experienced a robust positive precipitation trend during the twentieth century, which has continued into the first two decades of the twenty-first century (Liebmann et al. 2004; Haylock et al. 2006; Barros et al. 2008; Seager et al. 2010; Gonzalez et al. 2014; Vera and Díaz 2015; Zhang et al. 2016; Díaz and Vera 2017; Díaz et al. 2021). In particular, austral summer [December–February (DJF)] precipitation in SESA has increased substantially from the early twentieth century to the early twenty-first century, one of the largest such trends in the observational record (e.g., Liebmann et al. 2004; Haylock et al. 2006; Barros et al. 2008; Seager et al. 2010; Dai 2021). This DJF trend is the

principal contribution to the observed increase in total annual precipitation in SESA and has promoted agricultural expansion, increases in river flow, and increased vulnerability to flooding (Genta et al. 1998; Viglizzo and Frank 2006; Zhang et al. 2016).

These precipitation trends across SESA are consistent and robust across rain gauge data and gridded precipitation datasets (Carvalho 2020). For instance, Haylock et al. (2006) found increased precipitation totals and extremes based on rain gauge data in SESA between 1960 and 2000. These results corroborate one of the first assessments of precipitation trends in South America in which a positive summer precipitation trend was observed south of 20°S based on rain gauge and gridded precipitation datasets (Liebmann et al. 2004). Significant rainfall trends over the La Plata basin have been quantified, as have an increased number of rainy days and extreme daily precipitation in the southern region of the South Atlantic convergence zone (de Barros Soares et al. 2017; Zilli et al. 2017). These trends are also reflected in runoff records of downstream river flow rates after 1950 (Dai 2021).

Increases in precipitation over the SESA region have translated into important agricultural impacts, while the SESA region more generally is a vital agricultural area and relies heavily on hydroelectric power. Over the past several decades, Argentina's soy cultivation area increased by 210%, in large part because of increased precipitation that promoted crop production expansion into areas previously used for livestock (Magrin et al. 2005; Baldi and Paruelo 2008; Barreiro et al. 2014; Lucas et al. 2018). Similarly, southern Brazil includes most of the country's irrigated crops and has been one of the most productive agricultural

 Denotes content that is immediately available upon publication as open access.

Corresponding author: Arianna M. Varuolo-Clarke, ariannav@ldeo.columbia.edu

DOI: 10.1175/JCLI-D-20-0746.1

© 2021 American Meteorological Society. For information regarding reuse of this content and general copyright information, consult the AMS Copyright Policy (www.ametsoc.org/PUBSReuseLicenses).

zones in the world over the past few decades (Schnepf et al. 2001). Southern Brazil also produces a large share of rice and the state of Rio Grande do Sul is one of the most important regions for soybean production in the country (Schnepf et al. 2001; Zortea et al. 2018). In sum, Brazil, Argentina, and Paraguay are the second-, third-, and sixth-largest soybean producers globally, with Brazil and Argentina also being among the top 10 countries for maize and beef production (http://www.fao.org/faostat/en/#rankings/commodities_by_country).

Land-use and land-cover changes associated with the expanding agricultural practices in SESA are also likely to feed back on the regional climate, including precipitation patterns (e.g., Xue et al. 2006; Lee et al. 2011). Modeling experiments comparing simulations with and without vegetation changes indicate that land degradation is likely to have caused precipitation reductions over SESA during the period 1948–2010 (Chilukoti and Xue 2021). These results corroborate previous examinations of the influence of land-use and land-cover changes on precipitation in this region of South America (e.g., Xue et al. 2006; Lee et al. 2011; Salazar et al. 2015). These land-use impacts may therefore have worked to diminish the magnitude of the twentieth-to-twenty-first-century precipitation trends over SESA, thus indicating that work to separate the influence of anthropogenic land-use changes and anthropogenic emissions is an important further area of study.

Many factors indeed influence SESA precipitation, yet there is little consensus on the relative contributions to the positive twentieth-to-twenty-first-century precipitation trend from external forcing and internal oceanic and atmospheric variability (referred to collectively as internal variability hereinafter). Furthermore, prior analyses have shown the near inability of models to simulate the observed magnitude of the twentieth-to-twenty-first-century wetting trend (e.g., Seager et al. 2010; Gonzalez et al. 2014; Zhang et al. 2016). Analyses of historical simulations from general circulation models have suggested that radiative forcing due to increasing anthropogenic emissions of greenhouse gases (GHGs) promotes increased precipitation in SESA, but the forced trends are weaker than the observed trends (e.g., Vera and Díaz 2015; Zhang et al. 2016; Díaz and Vera 2017). The proposed mechanism is that increased GHGs drive tropical expansion, leading to a southward shift of the subtropical dry branch of the Hadley cell, moving it poleward of SESA, and thus promoting anomalous ascent that leads to increased rainfall over the region (Son et al. 2010; Arblaster et al. 2011; McLandress et al. 2011; Polvani et al. 2011; Zhang et al. 2016).

Stratospheric ozone depletion has been a major cause of atmospheric circulation changes over the Southern Hemisphere (SH) since 1960 (Thompson et al. 2000; 2011; Gonzalez et al. 2014). The ozone hole cooled the summer stratosphere over the southern polar region, promoting changes in geopotential heights and surface winds that manifest as a southward shift and strengthening of the midlatitude jet (Thompson and Solomon 2002; Gillett and Thompson 2003; Perlwitz et al. 2008; Son et al. 2008), also evident as a positive trend in the southern annular mode (SAM; Thompson et al. 2000) and a widening of the summertime Hadley circulation (Son et al. 2009). Gonzalez et al. (2014) found that the consequent impact of ozone depletion on SESA precipitation during austral summer has

been as large as, and perhaps larger than, the impact of increasing GHGs, but only after 1960.

The SAM is the leading mode of natural atmospheric circulation variability in the SH with varying seasonal impacts on SESA precipitation (Thompson et al. 2000; Marshall 2003; Thompson et al. 2011). These impacts are strongest during austral winter and late spring, but of opposite sign (Silvestri and Vera 2003). The SAM influence on SESA precipitation is not independent of El Niño–Southern Oscillation (ENSO) because ENSO influences SAM (L’Heureux and Thompson 2006; Dätwyler et al. 2020). The strongest link between SESA and SAM variability nevertheless occurs during austral winter and spring, making the interannual variability of SAM unlikely to contribute to the centennial trend in austral summer precipitation in SESA.

SESA precipitation is also strongly affected by sea surface temperatures (SST; Seager et al. 2010). ENSO exerts its strongest influence during austral spring and weakest during austral summer (Pisciottano et al. 1994; Grimm et al. 2000; Cazes-Boezio et al. 2003; Seager et al. 2010; Barreiro et al. 2014). However, ENSO is an unlikely driver of the secular trends in SESA summer precipitation: there is no observed trend toward El Niño–like conditions that would wet SESA and the strongest influence of ENSO on SESA precipitation is in austral spring not summer (Li et al. 2011; McGregor et al. 2013; Tindall et al. 2016; Grothe et al. 2020). These two considerations suggest that if a mode of oceanic or atmospheric variability has significantly contributed to the SESA precipitation trend, it is not likely to be directly associated with ENSO.

The Pacific Ocean also contributes to SESA precipitation variability on multidecadal time scales through the Pacific decadal oscillation (PDO; Mantua et al. 1997; Zhang et al. 1997; Mantua and Hare 2002) and the interdecadal Pacific oscillation (Folland et al. 1999; Power et al. 1999), which are closely related (Deser et al. 2004). Precipitation anomalies are strongest when the warm phase of the PDO and the warm phase of ENSO (El Niño) coincide, especially during January and February (Andreoli and Kayano 2005; Kayano and Andreoli 2007; Bonfils and Santer 2011; Kayano et al. 2020). The PDO is therefore a potential contributor to the twentieth-to-twenty-first-century precipitation trend in SESA, given its potential to imprint decadal variability in SESA precipitation.

Anomalies in tropical Atlantic Ocean SSTs forced by Atlantic multidecadal variability (AMV; Schlesinger and Ramankutty 1994; Kerr 2000; Enfield et al. 2001; Ting et al. 2009) are also significant contributors to low-frequency SESA hydroclimate variability (Seager et al. 2010). The negative AMV phase promotes wet conditions in SESA, while the positive phase promotes dry conditions (Seager et al. 2010). Seager et al. (2010) suggested that AMV variability is principally associated with the SESA precipitation trend and pointed out that the AMV transition to a positive phase since the late 1990s (e.g., Ting et al. 2009) could promote a return to drier conditions over the region.

The myriad factors listed above make it challenging to isolate any single factor, natural or forced, as the causal mechanism that drove the secular precipitation trend over the twentieth to twenty-first centuries in SESA. Here we build on prior work to provide a comprehensive assessment

of contributions from forced and internal variability to simulated twentieth-to-twenty-first-century precipitation trends in SESA. We perform this assessment across two model generations, including the first detailed characterization of how these trends are simulated in CMIP6 models. These simulations are evaluated against observed twentieth-to-twenty-first-century precipitation trends in SESA. Our results have critical implications for anticipated future hydroclimate trends and their consequent impacts on agriculture, hydroelectric power, and flooding risk over the SESA domain.

2. Data and methods

a. Observations

We use two datasets to assess observed precipitation in SESA: 1) the Climatic Research Unit 0.5°-resolution gridded precipitation dataset, version 4.04 (CRU TS v. 4.04; [Harris et al. 2020](#)), available from 1901 to 2019 and 2) the Global Precipitation Climatology Centre 0.5°-resolution precipitation dataset available from 1891 to 2016 (GPCC v2018; [Rudolf et al. 2010](#)).

b. Models

We compare two 16-member ensembles derived from CMIP3- and CMIP5-generation National Center for Atmospheric Research (NCAR) atmospheric models: the Community Climate Model, version 3 (CCM3; [Kiehl et al. 1998](#)), and the Community Atmosphere Model, version 5 (CAM5; [Neale et al. 2010](#)). Both ensembles are forced by globally observed SSTs derived from [Kaplan et al. \(1998\)](#) and Hadley Centre Sea Ice and SST (HadISST). Kaplan SSTs are specified over the tropical Pacific (20°S–20°N) from 1856 to 2012, whereas HadISST is used everywhere else from 1870 to 2012. Kaplan SSTs were used if available outside the tropical Pacific from 1856 to 1870, and climatological SSTs from HadISST were used otherwise ([Seager et al. 2005](#)); this adopted SST-forced configuration and subsequent model experiments are referred to as the Global Ocean Global Atmosphere (GOGA) simulations. The simulations are performed with an approximate 2.5° grid resolution and span 1856–2012.

Fully coupled historical simulations from 30 models within the CMIP5 archive, forced by historical trace gases, aerosol, solar, and volcanic forcing, are examined over 1901–2005 (information on the models is in [Table 1](#); [Taylor et al. 2012](#)). The CMIP5 ensemble includes the Community Earth System Model, version 1 (CESM), which is the fully coupled Earth system model developed by NCAR that uses CAM5 as the atmospheric model component. The standard CMIP5 CESM experiments are joined in our analysis by the NCAR CESM Large Ensemble (CESM-LENS), derived from over 40 integrations of CESM initialized after tiny perturbations are applied to the initial atmospheric temperature field in 1920 ([Kay et al. 2015](#)). Our analysis uses the first 35 members of the CESM-LENS because members 36–40 are known to be erroneously warm (see <http://www.cesm.ucar.edu/projects/community-projects/LENS/known-issues.html>; last access: 16 June 2020). All CESM-LENS runs are evaluated from 1920 to 2005.

TABLE 1. List of CMIP5 models and the number of runs used for the historical simulations. Expansions for many of these models can be found online (<https://www.ametsoc.org/PubsAcronymList>).

Models	Historical
BCC_CSM1.1	3
BCC_CSM1.1(m)	3
CESM1(BGC)	1
CESM1(CAM5)	3
CESM1(CAM5-FV)	4
CESM1(FASTCHEM)	3
CNRM-CM5	10
CNRM-CM5.2	1
CanESM2	5
EC-EARTH	1
FGOALS-g2	5
FGOALS-s2	3
GFDL CM3	5
GFDL-ESM2G	3
GFDL-ESM2M	1
GISS-E2-H	11
GISS-E2-H-CC	1
GISS-E2-R	16
GISS-E2-R-CC	1
HadGEM2-AO	1
IPSL-CM5A-LR	6
IPSL-CM5A-MR	3
IPSL-CM5B-LR	1
MIROC-ESM	3
MIROC-ESM-CHEM	1
MIROC5	5
MRI-CGCM3	5
MRI-ESM1	1
NorESM1-M	3
NorESM1-ME	1
Total	110

Fully coupled historical experiments (1901–2014) from 52 CMIP6 models are also evaluated with natural and anthropogenic forcings including trace gases, aerosols, volcanic eruptions, and solar variability ([Eyring et al. 2016](#)). CMIP6 projections for four Shared Socioeconomic Pathways (SSPs) are additionally analyzed over the 2015–2100 period ([O'Neill et al. 2017](#)). The SSP projections are based on emissions scenarios assuming a range of possible future trajectories in population, economics, urbanization, and technological development ([O'Neill et al. 2017](#)). The following SSPs are used: SSP1-2.6, a world focused on sustainable growth and equity with +2.6 W m^{−2} radiative imbalance; SSP2-4.5, a “middle of the road” estimate incorporating trends that broadly match historical patterns and +4.5 W m^{−2} radiative imbalance; SSP3-7.0, a fragmented world with a resurgence of nationalism resulting in +7.0 W m^{−2} radiative imbalance; and SSP5-8.5, in which rapid and unconstrained economic growth and energy consumption persist and a +8.5 W m^{−2} radiative imbalance occurs ([O'Neill et al. 2017](#); [Cook et al. 2020](#)). Respective subsets of 32, 33, 31, and 36 models are assessed for the SSP1-2.6–SSP1-8.5 experiments, all of which exist within the 52-model collection comprising the analyzed historical simulations ([Table 2](#)). Last, preindustrial control runs from CMIP6 are

TABLE 2. List of CMIP6 models and the number of runs used for the historical, preindustrial control (piControl) runs, and the future projections using the SSP scenarios from SSP1-2.6 to SSP5-8.5. Low-top models are denoted by superscript L, high-top models are denoted by superscript H, and models with interactive stratospheric chemistry are denoted by superscript H*.

Models	Historical	piControl (length; yr)	SSP1-2.6	SSP2-4.5	SSP3-7.0	SSP5-8.5
ACCESS-CM2 ^H	3	1 (500)	1	1	1	3
ACCESS-ESM1-5 ^L	10	1 (900)	3	3	3	3
AWI-CM-1-1-MR ^H	5	1 (500)	1	1	5	1
AWI-ESM-1-1-LR ^H	1	1 (100)				1
BCC-CSM2-MR ^L	3	1 (600)	1	1	1	1
BCC-ESM1 ^L	3	1 (451)				
CAMS-CSM1-0 ^L	3	1 (250)				
CanESM5 ^L	65	2 (451; 1000)	50	50	50	50
CanESM5-CanOE ^L	3	1 (501)	3	3	3	3
CAS-ESM2-0 ^L	4	1 (549)				
CESM2 ^L	11	1 (1200)			3	3
CESM2-FV2 ^L	3	1 (500)				5
CESM2-WACCM ^{H*}	3	1 (499)	1	5	1	
CESM2-WACCM-FV2 ^{H*}	3	1 (500)				1
CMCC-CM2-SR5 ^L	1	1 (500)			1	6
CNRM-CM6-1 ^{H*}	29	1 (500)	6	6	6	1
CNRM-CM6-1-HR ^{H*}	1	1 (300)	1	1	1	5
CNRM-ESM2-1 ^{H*}	10	1 (500)	5	5	5	
E3SM-1-0 ^{H*}	3	1 (500)				
E3SM-1-1 ^{H*}	1	1 (165)				
E3SM-1-1-ECA ^{H*}	1	1 (165)				
EC-Earth3 ^H	19	2 (501; 1255)	3	17	4	54
EC-Earth3-Veg ^H	6	1 (500)	4	4	4	5
EC-Earth3-Veg-LR ^L	3	1 (501)				
FGOALS-f3-L ^L	2	1 (501)	1	1	1	1
FGOALS-g3 ^L	3	1 (700)	1	1	1	4
FIO-ESM-2-0 ^L	3	—	3	3		3
GFDL-CM4 ^L	1	1 (500)		1		1
GFDL-ESM4 ^L	3	1 (500)	1	3	1	1
GISS-E2-1-G ^H	38	8 (100, 100, 165, 165, 201, 301, 345, and 851)	1	10	1	1
GISS-E2-1-G-CC ^H	1	1 (165)				
GISS-E2-1-H ^H	23	2 (301, 401)				
HadGEM3-GC31-LL ^H	4	1 (500)	1	1		4
HadGEM3-GC31-MM ^H	2	1 (500)				3
INM-CM4-8 ^L	1	1 (531)	1	1	1	1
INM-CM5-0 ^H	10	1 (1201)	1	1	5	1
IPSL-CM6A-LR ^H	32	2 (250, 1200)	1	11	11	6
KACE-1-0-G ^H	3	1 (150)	3	3	3	3
MCM-UA-1-0 ^L	2	1 (500)	1	1	1	1
MIROC-ES2L ^L	10	1 (500)	3	1	1	1
MIROC6 ^H	50	1 (800)	3	3	3	50
MPI-ESM-1-2-HAM ^H	2	1 (780)				
MPI-ESM1-2-HR ^H	10	1 (500)	2	2	10	2
MPI-ESM1-2-LR ^H	10	1 (1000)	10	10	10	10
MRI-ESM2-0 ^{H*}	6	2 (251, 701)	1	1	5	2
NESM3 ^L	5	1 (500)	1	2		2
NorCPM1 ^L	30	3 (500, 500, 500)				
NorESM2-LM ^L	2	1 (110)	1	3	1	1
NorESM2-MM ^L	1	1 (500)	1	1	1	1
SAM0-UNICON ^L	1	1 (700)				
TaiESM1 ^L	1	1 (500)				
UKESM1-0-LL ^{H*}	17	1 (750)	5	5	5	5
Total	52 models (467 runs)	51 models (65 runs)	32 models (126 runs)	33 models (162 runs)	31 models (149 runs)	36 models (245 runs)

TABLE 3. Trends calculated as percent per decade on standardized precipitation data and the slope on the precipitation data (without standardization and in units of millimeters per month per year; in parentheses) for CRU and GPCC over the periods indicated. Boldface values highlight those trend that pass Mann–Kendall significance testing at the 95% threshold.

Time period	1901–2019 (2016)	1950–2019 (2016)	1920–2005	1920–2014
<i>CRU</i>				
Annual	+1.6 (+0.14)	+1.7 (+0.20)	+2.0 (+0.18)	+1.7 (+0.15)
DJF	+2.0 (+0.23)	+2.1 (+0.25)	+2.4 (+0.28)	+2.3 (+0.26)
MAM	+1.5 (+0.14)	+2.3 (+0.25)	+2.6 (+0.23)	+1.7 (+0.16)
JJA	+0.59 (+0.04)	−0.41 (−0.02)	+0.87 (+0.06)	+0.34 (+0.02)
SON	+1.6 (+0.14)	+1.9 (+0.20)	+1.8 (+0.18)	+1.6 (+0.14)
<i>GPCC</i>				
Annual	+1.3 (+0.11)	+1.9 (+0.19)	+1.9 (+0.16)	+1.5 (+0.13)
DJF	+1.7 (+0.18)	+2.5 (+0.3)	+2.1 (+0.22)	+2.0 (+0.2)
MAM	+0.95 (+0.08)	+1.8 (+0.2)	+2.2 (+0.19)	+1.4 (+0.11)
JJA	+0.83 (+0.05)	+0.18 (−0.004)	+1.0 (+0.07)	+0.52 (+0.04)
SON	+1.5 (+0.13)	+2.3 (+0.21)	+1.9 (+0.19)	+1.7 (+0.13)

also analyzed. Of the 51 CMIP6 models considered, some models have multiple ensemble members that vary in the length of the simulation and/or the parameterizations. In total, 65 total preindustrial simulations are analyzed from 51 of the 52 CMIP6 models. Information on all CMIP6 simulations is presented in Table 2; the selection of models and simulations for all of the above experiments was based on the current availability of data in the CMIP6 database.

c. Methods

Linear trends in precipitation are calculated for observations and model simulations. For CRU and GPCC, trends are calculated from 1902 to 2019 (2016 for GPCC), from 1950 to 2019 (2016 for GPCC), from 1921 to 2005, and from 1921 to 2014 (Table 3). The latter two intervals are for comparisons with modeled trends. Sliding trends are also calculated for the observations in 85-yr moving windows incremented by 1 yr over the 1902–2019 or 2016 period to estimate the spread in the observed trend over the observational interval. The developed framework allows us to compare the simulated trends with the observed spread of trends rather than just the one instance of a trend observed in both datasets. The 85-yr window is chosen for direct comparison with the CMIP5 generation of models, constrained by the CESM-LENS 1920–2005 period, and the CMIP6 SSP projections (2015–2100). Sliding 85-yr trends are also calculated in the preindustrial control runs. To test for the robustness of the observed precipitation trends, Mann–Kendall significance tests are employed using 95% as the significance threshold (Hamed 2008).

3. Results

a. Seasonal and temporal variability of the observational SESA precipitation trend

The annual observed SESA precipitation climatologies according to CRU and GPCC are shown in Fig. 1a. The rainy season is October–May, and we focus specifically on DJF, the wettest average 3-month period (when ~32% of the total annual precipitation falls). Secular positive precipitation trends

extend from October to March and are centered in the DJF rainy season (Fig. 1b). Across CRU and GPCC all of the precipitation trends in DJF are significant. The seasonal trends for CRU over 1901–2019 are plotted geographically in Fig. 2, for all of South America with the SESA region indicated by the black-outlined boxes and stippling over regions where the trend does not pass the 95% significance threshold. The DJF trend (Fig. 2b) occurs across almost all of SESA, is significant throughout most of the region and also is reflected strongly in the annual precipitation trends (Fig. 2a). Positive but smaller trends that do not pass the 95% significant threshold also occurred in autumn [March–May (MAM); Fig. 2c] and spring [September–November (SON); Fig. 2e], whereas austral winter [June–August (JJA); Fig. 2d] had no trend. The strong positive DJF precipitation trend is also clearly evident in the mean SESA precipitation in both the CRU and GPCC datasets, with statistically significant linear increases of ~27% and ~22% from 1902 to 2019 and from 1902 to 2016, respectively (Fig. 3).

Data coverage over SESA reduces dramatically prior to 1945, and differences in how missing data are estimated likely account for much of the differences between the GPCC and CRU trends (Fig. 3). Particularly with regard to the calculated trends, these differences contribute to a slightly more muted trend estimate in the GPCC dataset relative to CRU. Given these uncertainties prior to 1945, we evaluate the robustness of the estimated trends. Our general approach is to test whether the inclusion of pre-1945 data significantly affects our estimates of the linear trends. Figure 4 presents the geographic trends of DJF precipitation in CRU and GPCC from 1902 to 2019 (2016 for GPCC) and from 1950 to 2019 (2016 for GPCC). The trends over the shorter interval compare well to the trends over the longer interval in terms of spatial features and magnitudes; however, the area in which the trends are significant over the short periods is much smaller than the area where significant trends occur over the longer period. Table 3 provides trend values (and Mann–Kendall significance testing) calculated for CRU and GPCC over the periods 1901–2019 (2016 for GPCC), 1950–2019 (2016 for GPCC), 1921–2005, and 1921–2014. The latter two periods have been included because of subsequent

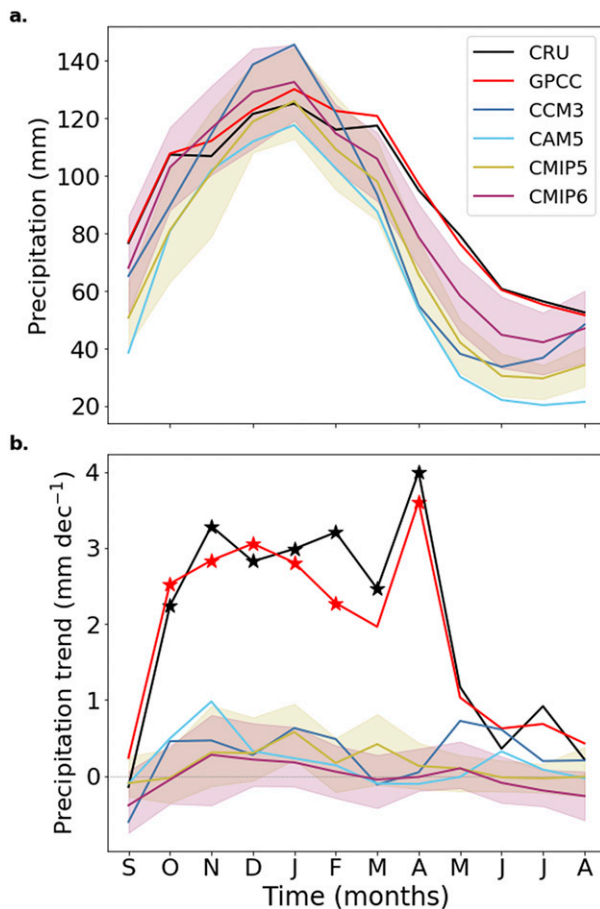


FIG. 1. (a) Annual climatology of SESA precipitation, and (b) monthly linear trends calculated for observations and climate model simulations. The model climatologies are determined from ensembles of simulations from the CCM3 and CAM5 historical SST-forcing experiments and from the CMIP5 (not including CESM-LENS) and CMIP6 fully coupled historical experiments. Shaded regions represent the interquartile range between the 25th and 75th percentiles across the CMIP5 and CMIP6 multimodel means. The periods over which the climatologies were determined were: 1901–2019 (CRU), 1901–2016 (GPCC), 1901–2012 (CCM3 and CAM5), 1901–2005 (CMIP5), and 1901–2014 (CMIP6). Monthly trends are calculated from 1920 to 2005 for all data. The stars in (b) indicate where the monthly observed trends pass the Mann-Kendall test at the 95% significance level. The model simulations pass the Mann-Kendall test in less than 5% of the assessed months.

comparisons with model estimates of precipitation over SESA. Over all intervals, the annual, DJF, and SON trends over SESA are positive, of similar magnitude, and statistically significant. Given the similarities between the trends calculated in the two datasets whether or not pre-1945 data are used, we employ all available data for subsequent precipitation trend analyses but factor in the observational data uncertainties, as represented by the different trend estimates from the CRU and GPCC data.

As a final assessment of the observational data, we note that the SESA summer precipitation time series in Fig. 3 does not

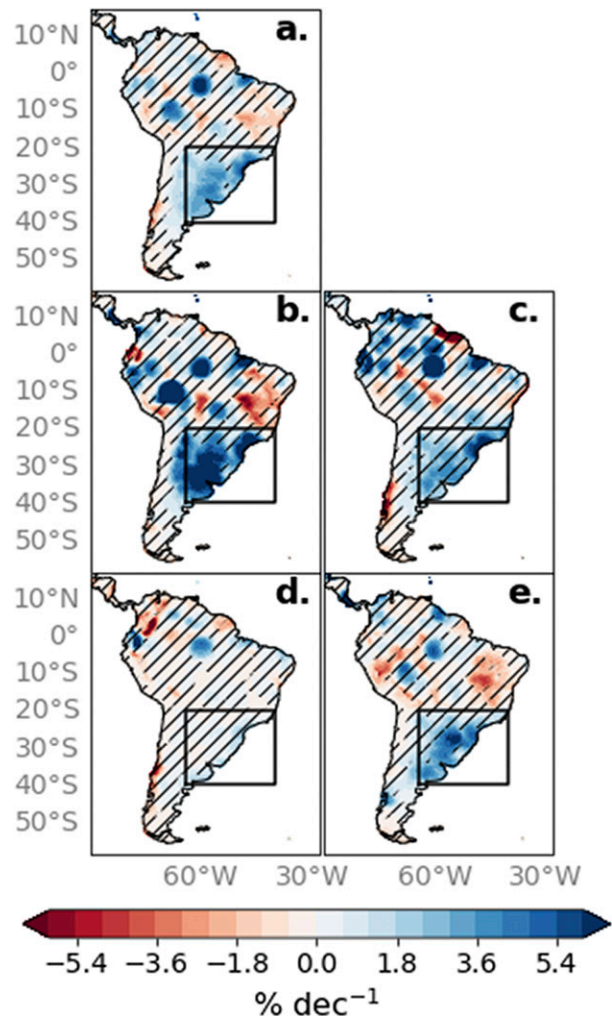


FIG. 2. Geographic linear precipitation trends calculated for annual and seasonal CRU precipitation averages: (a) annual, (b) DJF, (c) MAM, (d) JJA, and (e) SON. Trends are calculated as the relative change per decade (% decade⁻¹) from 1901 to 2019. Black-outlined boxes bound the SESA region; only precipitation over the land area is used for the analysis. Stippling denotes where the trend is not significant as based on a Mann-Kendall test and a 95% significance threshold.

include the twenty-first-century downturn in SESA summer precipitation reported by Zhang et al. (2016). This difference arises because Zhang et al. (2016) use the November–April (NDJFMA) window to characterize SESA summer precipitation, whereas we use DJF. Zhang et al. (2016) also analyzed data through 2012 whereas our analysis extends through 2019. Figure 5 plots monthly precipitation from the CRU TS 4.04 time series in SESA from November through April, the 9-yr running mean of monthly precipitation, and the 9-yr running mean of NDJFMA average SESA precipitation, the latter of which is consistent with Zhang et al. (2016). The downturn in precipitation is most pronounced in March and April, is more weakly expressed in November–January, and is absent

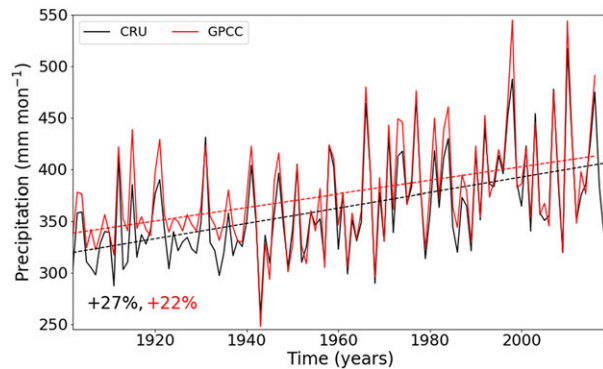


FIG. 3. Observed total precipitation for the DJF season estimated from the CRU (black; 1902–2019) and GPCC (red; 1902–2016) datasets over the SESA domain shown in Fig. 2. Dashed lines show the calculated linear trends for each of the datasets, and the numbers in the lower-left-hand side of the panel correspond to the calculated trends as the total percent change in DJF precipitation over the full time period of each dataset. Both time series pass the Mann–Kendall test at the 95% significance level.

in February. In nearly all months, there is a rebound in precipitation after 2012 that is reflected in the running NDJFMA mean. Consequently, the early-2000s downturn in SESA precipitation during NDJFMA was a temporary decadal departure from the secular trend, in line with Zhang et al. (2016), who argue it was associated with internal variability. Furthermore, the decadal downturn is most weakly expressed in DJF precipitation and does not change the significance of the calculated trend for that season. We therefore proceed to use the DJF window for our analyses given its representation of the core period of austral summer precipitation, and the associated trend, in the region.

b. Is the wetting trend driven by SSTs?

The ensemble mean of the SST-forced simulations from CCM3 and CAM5 allows an assessment of how much the SESA hydroclimate variability and secular trend are driven by global SSTs, whether through internal ocean variability or radiatively forced changes reflected in the SSTs. The annual climatological cycle of SESA precipitation is generally well represented in the CCM3 and CAM5 ensembles (Fig. 1a). Both ensembles correctly simulate the wettest month to be in January, whereas the CCM3 ensemble simulates a wetter austral summer than observed or simulated by CAM5; both models simulate drier austral winter conditions than observed. Small differences notwithstanding, there is overall agreement between the observations and the models in the timing, the relative amplitudes of the wet and dry seasons, and the average precipitation in each month.

Despite the climatological comparisons, neither model simulates DJF precipitation trends that are nearly as strong as observed (Figs. 1b and 6a). The trend maps for the models (Figs. 6b,c) indicate that the weak tendency toward positive simulated SESA precipitation trends are not attributable to a geographic displacement of wetting regions. The models also do

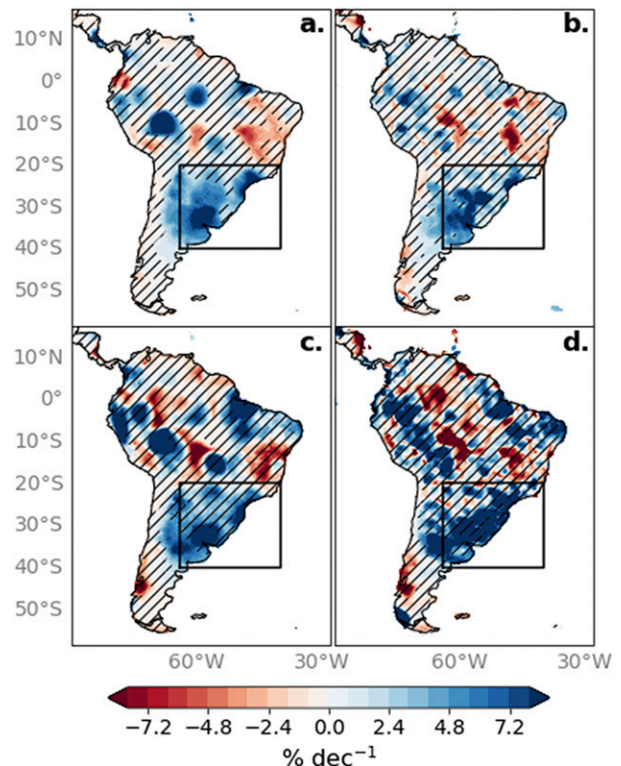


FIG. 4. Geographic DJF linear trends calculated in (a) CRU from 1902 to 2019, (b) GPCC from 1902 to 2019, (c) CRU from 1950 to 2019, and (d) GPCC from 1950 to 2016 as the relative change per decade ($\% \text{ decade}^{-1}$). Black-outlined boxes bound the SESA region; land area is used only. Stippling denotes where the trend is not significant as based on a Mann–Kendall test and a 95% significance threshold.

not simulate the positive precipitation trends in the autumn and spring months (Fig. 1b). Furthermore, the interquartile range (not shown) of the ensembles indicates that there is no overlap between DJF trends in the individual ensemble members and observations, thus indicating that the observed trends are outside the range of internal atmospheric variability within the models for this period.

The SST-forced trends are further compared with observations in Fig. 7, which displays boxplots for the trends and associated uncertainty range of the observational datasets and the ensemble spread in the trends across the 16-member ensembles from CCM3 and CAM5 models. We additionally calculate the CRU and GPCC trend from 1921 to 2005 to facilitate model comparisons with the specific 85-yr interval spanned by the CCM3 and CAM5 experiments (stars in Fig. 7). The median trend in each boxplot for the models represents the forced SST response over SESA, with the spread of the distribution characterizing the influence of modeled internal atmospheric variability. The mean SESA precipitation trend from 1921 to 2005 in both SST-forced experiments is less than 25% of the 1921–2005 observed trend in both CRU and GPCC. The trend over 1921–2005 is 2.4% and 2.1% decade^{-1} in CRU and GPCC but only 0.43%

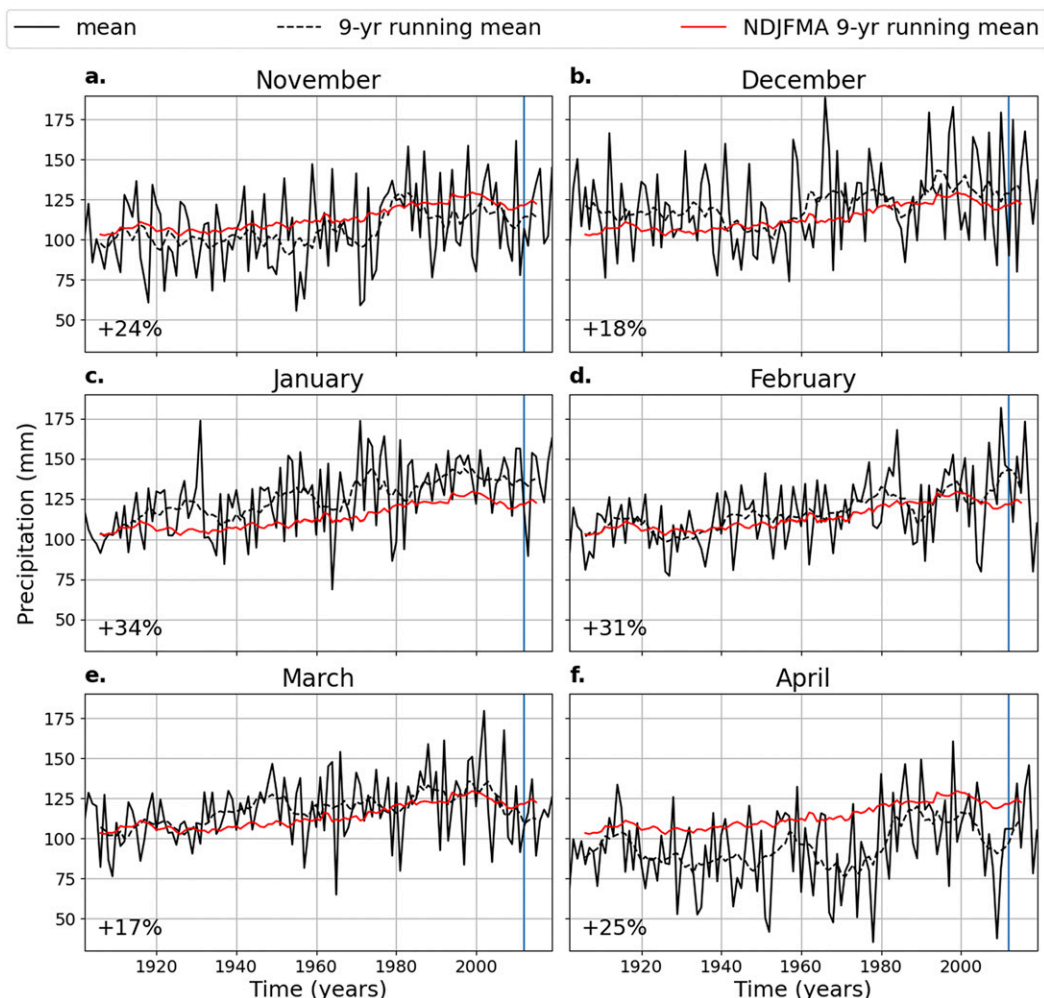


FIG. 5. Monthly SESA precipitation time series from CRU TS 4.04 calculated as the area-weighted average of the land region in the black-outlined boxes in Fig. 2. Data are shown for each month in the NDJFMA window over 1901–2019. Nine-year running means are shown for each of the individual monthly time series, and the NDJFMA 9-yr running mean, parallel to what was calculated in Zhang et al. (2016), is provided in each of the panels for reference. The values in the bottom-left corner of each panel are the total percent change for each season from 1901 to 2019. The blue vertical line marks 2012, which was the last year included in the Zhang et al. (2016) analysis.

and $0.23\% \text{ decade}^{-1}$ in CCM3 and CAM5. Additionally, none of the ensemble members from either model produces trends that even approach the magnitude of those in the lower uncertainty range of the observations.

The implication of the SST-forced experiments, if taken at face value, is that SST variability as realized over the historical interval cannot explain the observed trend over SESA. This conclusion, however, assumes that the CCM3 and CAM5 models realistically simulate atmosphere–ocean coupling, atmospheric teleconnections, and the strength of internal variability. Additionally, the precipitation trend in SESA may have been forced by impacts of anthropogenic emissions on atmospheric circulation that are not included, or poorly represented, in the SST-forced models. To address these additional possibilities, we turn in the subsequent sections to

analyses of the fully coupled historical simulations from CMIP5 and CMIP6.

c. Is the wetting trend driven by anthropogenic forcing?

The fully coupled historical simulations in CMIP5 and CMIP6 allow an assessment of the possible influence of atmosphere–ocean coupling, anthropogenic emissions, and internal atmosphere–ocean variability that could not be assessed in the SST-forced simulations. These fully coupled simulations include GHG forcing as well as aerosol forcing, land-use change, and stratospheric ozone depletion (Taylor et al. 2012; Eyring et al. 2016). Some of the models include high-top atmospheric models (defined as having a model top height $< 1 \text{ hPa}$), which allows an assessment of the impact of stratospheric dynamics on SESA precipitation variability given the established influence

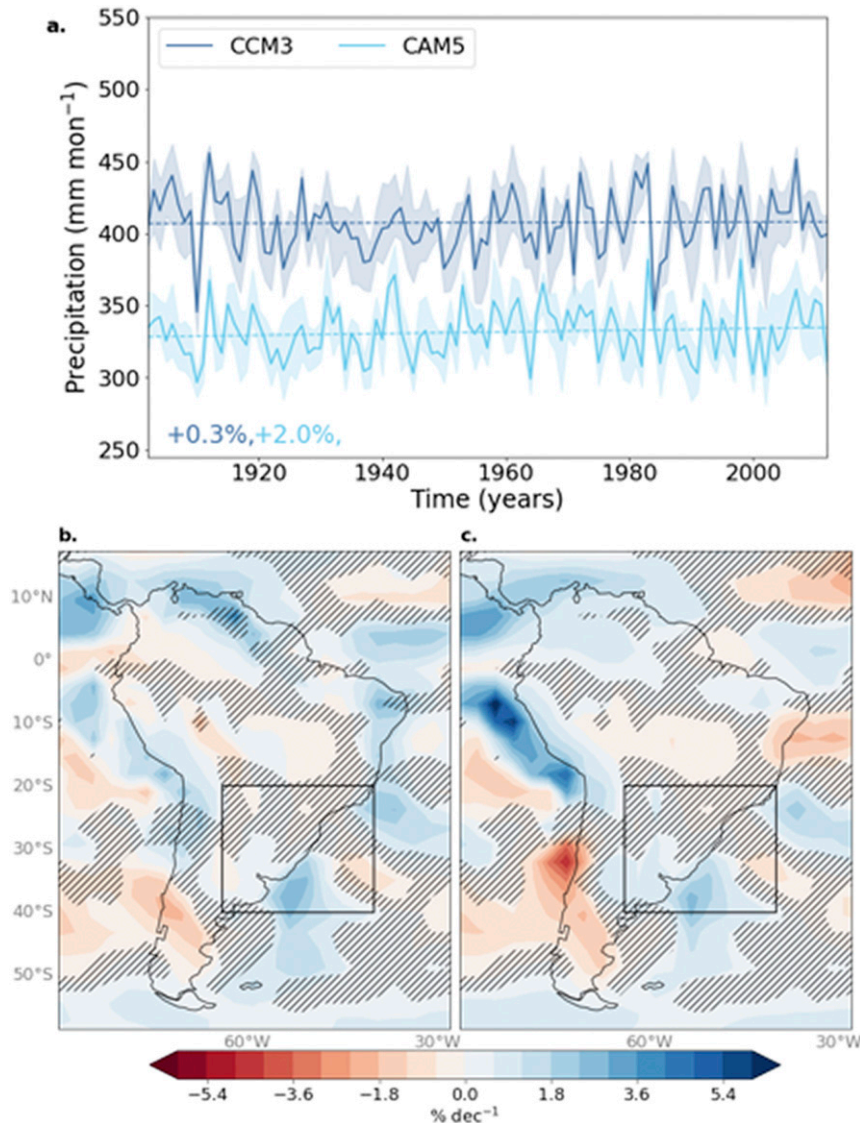


FIG. 6. (a) Simulated ensemble mean DJF precipitation totals (mm month^{-1}) from CCM3 and CAM5, both over the period 1902–2012; shading represents the interquartile spread across the respective ensembles. Dashed lines show the calculated linear trends for each model's ensemble mean, and the numbers in the lower-left-hand side of the panel correspond to the calculated trends as the total percent change in DJF precipitation from 1902 to 2012. One ensemble member from CAM5 simulates a SESA precipitation trend that passes the Mann–Kendall test at the 95% significance level, whereas the rest of the members in the CAM5 ensemble and all of the CCM3 ensemble members simulate trends that do not pass the significance test. Also shown are geographic trends calculated for the ensemble mean DJF precipitation in (b) CCM3 and (c) CAM5 as the relative change per decade ($\% \text{dec}^{-1}$). The black-outlined box bounds the SESA region, in which only precipitation over land area is used for the analysis. Stippling indicates where fewer than 12 ensemble members agree on the sign of the trend. Where there is no stippling, 12 or more ensemble members agree on the sign of the trend.

of stratospheric ozone depletion on the precipitation trend since 1960 (e.g., [Gonzalez et al. 2014](#)). A subset of the high-top models includes interactive stratospheric chemistry schemes, which may further impact model simulations of SESA precipitation trends.

Collectively, we do not perform an attribution of the individual forcings herein, but instead assess the collective influence of the incorporated forcings within the fully coupled all-forcing simulations. Additionally, relative to the SST-forced simulations, the

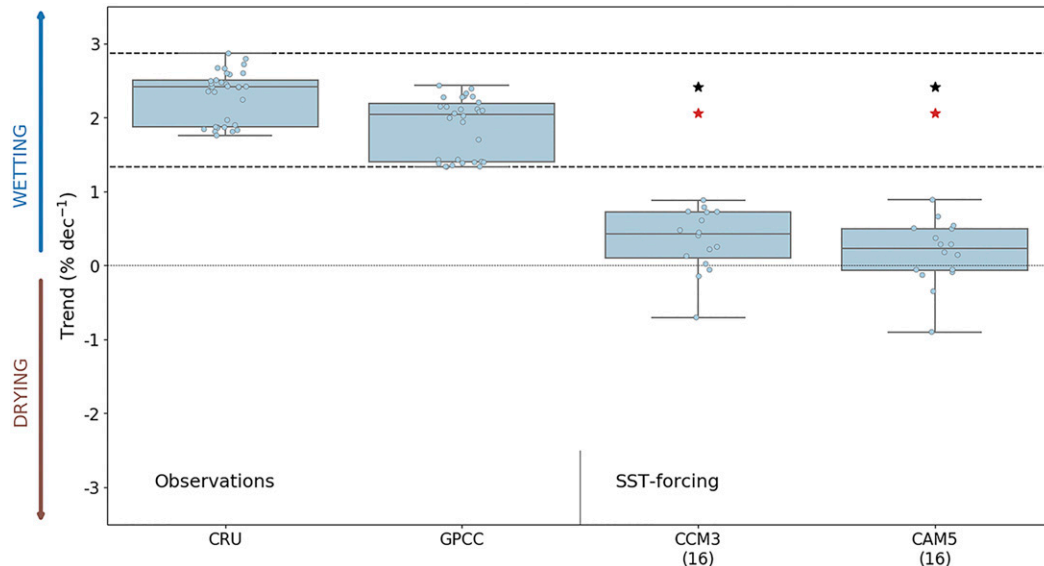


FIG. 7. Boxplots of linear trends in SESA DJF precipitation calculated as the relative change ($\% \text{dec}^{-1}$) for CRU, GPCC, CCM3, and CAM5. Observational boxplots represent the distributions for sliding 85-yr trends calculated from 1902 to 2019 (CRU) or 2016 (GPCC). The black and red stars represent specifically the 1921–2005 trend values in the CRU and GPCC datasets, respectively. All simulated trends are over 1921–2005. The dashed horizontal lines represent the minimum and maximum thresholds of the observational uncertainty as based on the minimum GPCC trend and the maximum CRU trend, which are 1.36% and $2.86\% \text{dec}^{-1}$, respectively. Internal black lines in each boxplot represent the median value of the distribution, the box outlines the interquartile range, and the whiskers are defined as 1.5 times the interquartile range. The numbers underneath the labels indicate the number of simulations in the CCM3 and CAM5 ensembles.

fully coupled models should have a wider range of internal variability due to the presence of atmosphere–ocean coupling, which is also assessed.

Figure 8 presents the distributions of SESA precipitation trends simulated in the CMIP5 and CMIP6 historical experiments and their multimodel means. The forced multimodel mean trend in CMIP5 is $0.25\% \text{dec}^{-1}$, falling between the CCM3 and CAM5 SST-forced trends (0.43% and $0.23\% \text{dec}^{-1}$, respectively). The CMIP6 forced multimodel mean trend is weaker than CMIP5 (and the SST-forced simulations) at $0.12\% \text{dec}^{-1}$ over 1921–2005. The CMIP6 anthropogenic forced trend is $0.17\% \text{dec}^{-1}$ when the trends are calculated through 2014 and still weaker than CMIP5. The historical simulations are further broken down by individual model in Fig. 8 and compared with the observational range of uncertainty, defined by the minimum GPCC trend and the maximum CRU trend; this range is 1.36% – $2.84\% \text{dec}^{-1}$ based on the 85-yr sliding-window trends calculated across GPCC and CRU for 1902–2016 and 1902–2019, respectively. Across both ensembles, it is clear that, while the ensemble-mean forced response is positive, there is a large discrepancy in the magnitude and even sign of the trend among the individual models. None of the median ensemble values of the individual model distributions is as large as the observed values for the 1921–2005 period, denoted by the black and red markers in the CMIP5 and CMIP6 panels, respectively. For the CMIP5 ensemble, just 2.76% of the 145 simulations fall within the observed range of uncertainty while 1.28% of the 467 CMIP6 simulations fall

within the observed range of uncertainty (Fig. 8). The CMIP6 forced trends are thus weaker than those in the CMIP5 ensemble and even more inconsistent with the observed trends. This tendency toward weaker trends in CMIP6 is not simply due to the larger number of models and ensemble members in the CMIP6 archive. In a bootstrapped comparison in which 31 models and one run per model are randomly sampled 10 000 times from each archive, the CMIP5 31-model mean trend is higher than the CMIP6 31-model mean trend $\sim 80\%$ of the time.

Previous studies have suggested that the difference between the observed and simulated trends may be the consequence of either underestimated forced responses or underestimated low-frequency internal variability in the models (e.g., Seager et al. 2010; Gonzalez et al. 2014; Vera and Díaz 2015; Zhang et al. 2016; Díaz and Vera 2017; Díaz et al. 2021). Large individual model ensembles within the CMIP5 and CMIP6 suites allow forced responses to be estimated for individual models, but there is a lack of agreement even on the sign of the forced trend response in SESA. In CMIP6, there are 16 models that include at least 10 ensemble members in the historical experiment, affording the opportunity to estimate the forced response more robustly for those models. Within these 16 model ensembles, 6 models simulate forced negative trends over the historical period. While there are fewer such large ensembles available for CMIP5, the largest and most widely used large ensemble from CMIP5, the CESM LENS, also estimates a negative forced precipitation trend over SESA. These results corroborate the findings discussed in Gonzalez et al. (2014)

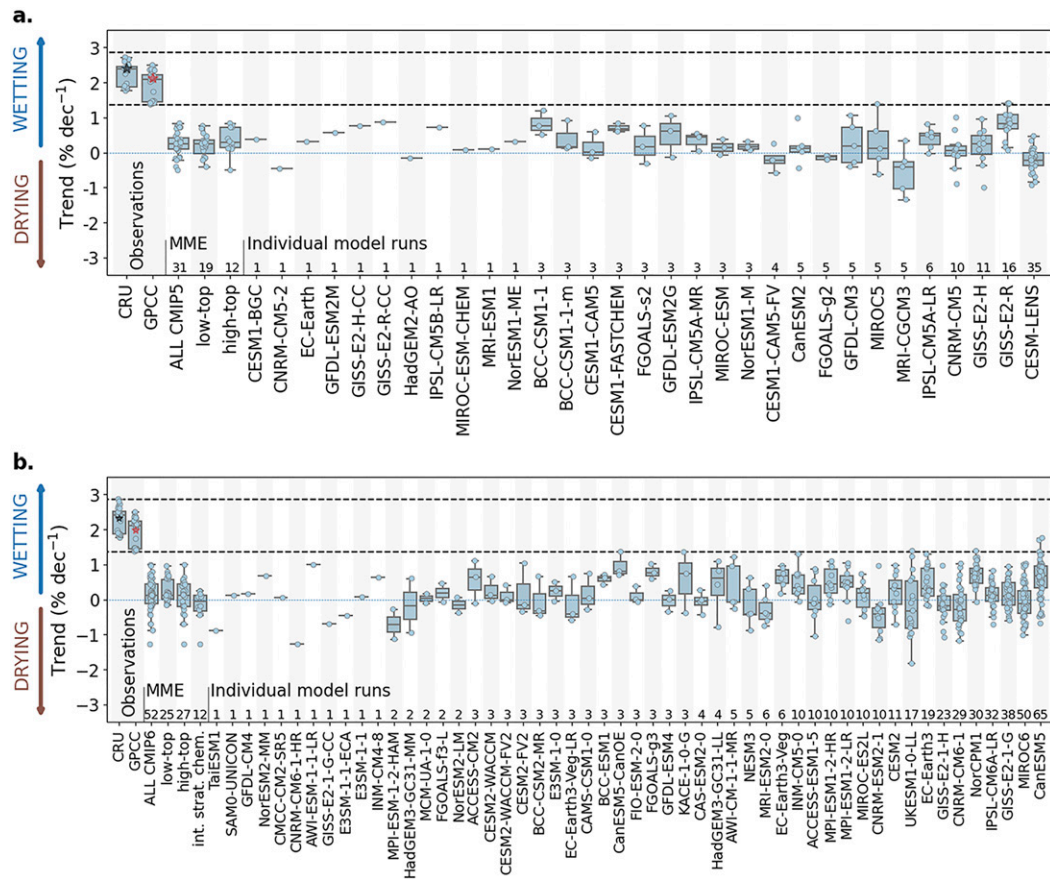


FIG. 8. Boxplots of linear trends in SESA DJF precipitation calculated as the relative change ($\% \text{ decade}^{-1}$) for historical simulations in (a) CMIP5 and (b) CMIP6, both from 1921 to 2005. The black (CRU) and red (GPCC) markers in each plot are the 1921–2005 trends, which allow for direct comparison with the models. The black dashed horizontal lines represent the minimum and maximum thresholds of the observational uncertainty based on the full spread of observations between the minimum GPCC trend and the maximum CRU trend, which are 1.36% and $2.86\% \text{ decade}^{-1}$ for the 1902–2019 or 1902–2016 periods. Internal black lines in each boxplot represent the median value of the distribution, the box outlines the interquartile range, and the whiskers are defined as 1.5 times the interquartile range; trends that fall outside this latter range are considered to be outliers. The numbers above each model name indicate the number of models included in the multimodel ensemble (MME) or the number of members included in an individual model ensemble. The gray-and-white-striped background is for visualization only.

where 8 of 26 CMIP5 models produce negative trends across a similar region from 1960 to 1999. These model details collectively place more doubt on even the sign of the forced precipitation response over SESA as simulated in the CMIP5 and CMIP6 models.

The CMIP5 and CMIP6 multimodel means are also broken down into low-top versus high-top models in Fig. 8 to address the influence of ozone depletion on SESA precipitation change. Based on previous literature regarding the influence of stratospheric influences on precipitation over SESA, high-top models might be expected to simulate trends that better compare with observations because they may better resolve the influence of stratospheric ozone depletion on tropospheric circulation (e.g., Son et al. 2010; Gonzalez et al. 2014). As indicated in Fig. 8, however, there is no clear indication that this

is so. In fact, the forced response indicated by the CMIP6 high-top models is similar to that of the low-top models, but with the high-top models exhibiting larger variability. Twelve of the CMIP6 high-top models also include interactive stratospheric chemistry and are further broken into a model subset in Fig. 8. These models simulate trends centered about zero with weaker maximum trends than indicated by the full spread of the CMIP6 multimodel ensemble means, further indicating that more accurate representations of stratospheric dynamics and chemistry do not yield trends or variability that better compare with observations.

As anthropogenic GHG emissions continue, the wetting trend in SESA is projected to continue as one of the most pronounced precipitation trends globally (Cook et al. 2020). The SSP projections included in CMIP6 allow assessment of

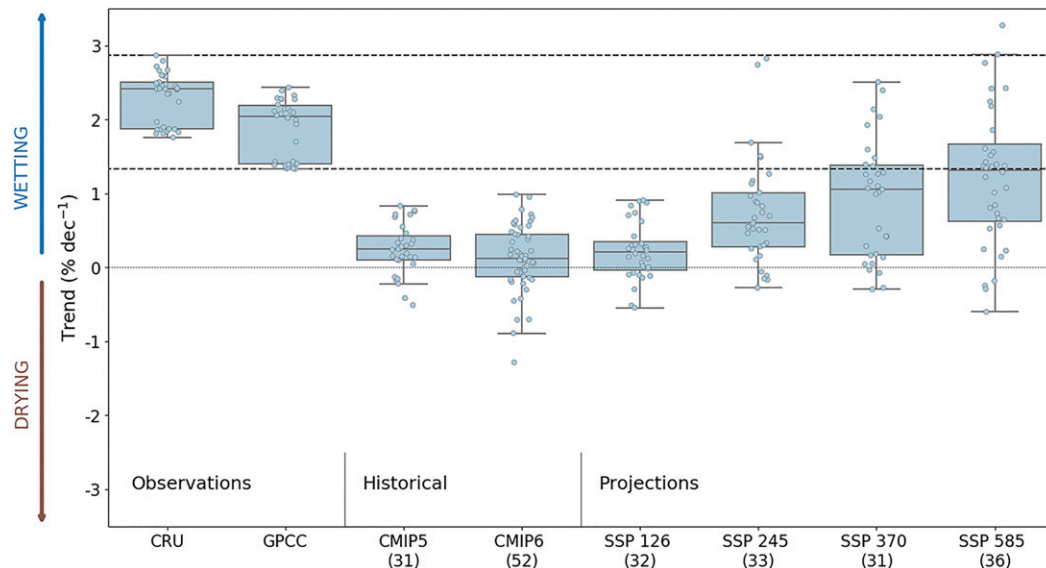


FIG. 9. Boxplots of linear trends in SESA DJF precipitation calculated as the relative change ($\% \text{dec}^{-1}$) for CRU, GPCC, and the simulated forced trends from CMIP5 and CMIP6 historical simulations, as well as the CMIP6 projections SSP1-2.6, SSP2-4.5, SSP3-7.0, and SSP5-8.5. Observational boxplots represent the distributions for sliding 85-yr trends calculated from 1902 to 2019 (CRU) or 2016 (GPCC). CMIP5 and CMIP6 historical trends are calculated from 1921 to 2005. Trends in SSP projections are calculated from 2016 to 2100. The values in parentheses below the model labels indicate the number of models included in the respective analysis. Internal black lines in each boxplot represent the median value of the distribution, the box outlines the interquartile range, and the whiskers are defined as 1.5 times the interquartile range; trends that fall outside this latter range are considered to be outliers.

the simulated precipitation trends in CMIP6 across different forcing pathways in comparison with the historical forcing (Fig. 8). There is a clear increase in simulated precipitation trends as emissions within the scenarios increase (Fig. 9) from SSP1-2.6 (lowest emissions) to SSP5-8.5 (highest emissions). The CMIP6 models therefore do simulate a wetting response to GHG forcing that appears to be a continuation and intensification of the small (and ambiguous) trends in the historical simulations. Despite the very strong and increasing GHG forcings imposed in SSP5-8.5, however, the magnitude of the multimodel median trend is still weaker than the observed twentieth-to-twenty-first-century trend. One possible explanation is that the model response to anthropogenic radiative forcing is too weak. An alternative explanation might be that the observed trend is due to internal variability, which is underrepresented in the models.

d. Is the SESA precipitation trend consistent with modeled internal variability?

To see whether the inability of models to simulate the observed trends is because of an underestimate of low-frequency internal variability, we calculate SESA trends as 85-yr sliding-window trends incremented by 1 yr over the full length of each preindustrial control run for CMIP6. Only 11 of 65 preindustrial control runs ever simulate a trend in DJF SESA precipitation that falls within the observed range and none of the runs ever simulates an 85-yr trend as strong as the median observed 85-yr sliding-window trend within the CRU dataset from 1902

to 2019 (Fig. 10). Two models (CNRM-ESM2-1 and GISS-E2-1-H) simulate a single 85-yr trend approximately equal to the GPCC mean estimate.

The observed trend is ultimately some combination of a specific realization of internal variability and anthropogenic forcing. However, when we add the CMIP6 multimodel ensemble forced response of $0.12\% \text{dec}^{-1}$ to the trends calculated for the preindustrial control runs (not shown), it is very rare that this modeled combination of forced trend and internal variability ever produces a precipitation trend as strong as observed. Adding the multimodel forced trend to the 65 preindustrial simulations results in an additional five simulations that ever realize an 85-yr trend that falls within the observed range of uncertainty (bringing the total to 16 simulations out of 65). Yet there is still no simulation with an 85-yr trend as strong as the observed median 85-yr trend based on the CRU dataset (not shown).

The explanation for the near inability of the models to simulate observed trends is ambiguous because the models may simulate either too small of a forced response and/or underestimate precipitation trends generated by internal variability. However, the SST-forced experiments we evaluated, which include the specific realization of internal oceanic variability over the twentieth to twenty-first centuries, still do not achieve simulated trends that are comparable to the observations, potentially pointing to an undersampling of internal atmospheric variability in the models as the reason for the underestimated simulated trends. Further in-depth

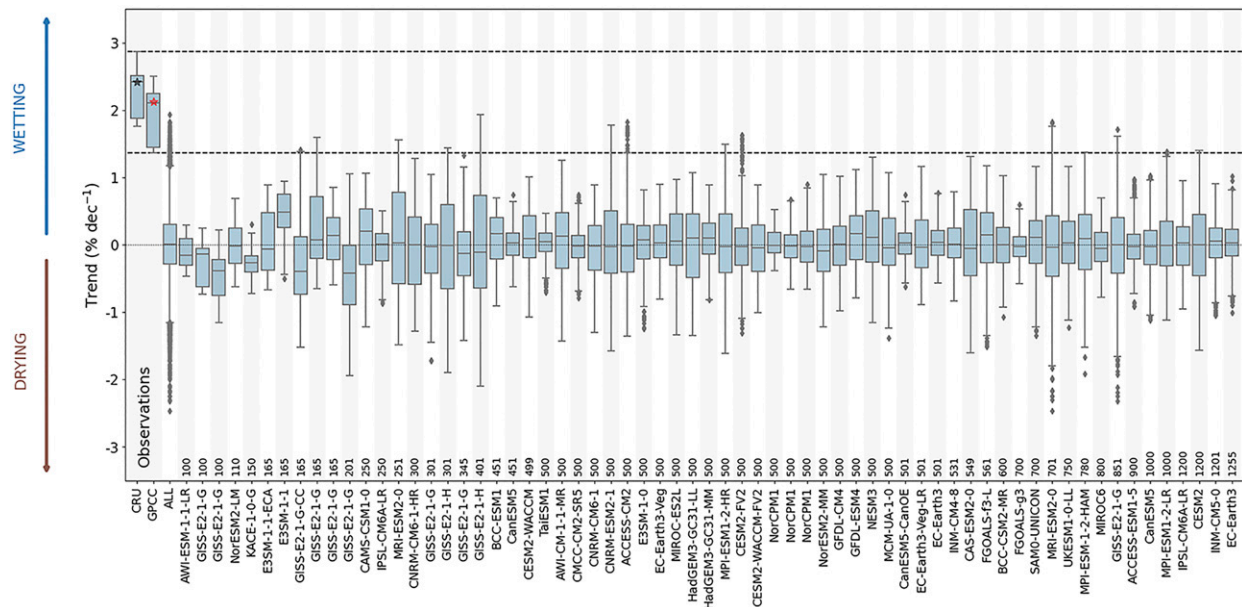


FIG. 10. Boxplots of the linear 85-yr sliding-window trends in SESA DJF precipitation calculated as the relative change ($\% \text{ decade}^{-1}$) for the CMIP6 preindustrial control runs. The models are ordered by length of control run, ranging from 100 to 1255 years. The black and red stars represent specifically the 1921–2005 trend values in the CRU and GPCC datasets, respectively, and the 85-yr sliding-window trends from 1902 to 2019 or 2016 are presented in the boxplot. The dashed horizontal lines represent the minimum and maximum thresholds of the observational uncertainty as based on the full spread of observations between the minimum GPCC trend and the maximum CRU trend, which are 1.36% and $2.86\% \text{ decade}^{-1}$. Internal black lines in each boxplot represent the median value of the distribution, the box outlines the interquartile range, and the whiskers are defined as 1.5 times the interquartile range; trends that fall outside this latter range are considered to be outliers. Outliers are indicated by gray diamonds. The numbers above each model name indicate the length of the simulation (yr). The gray-and-white-striped background is for visualization only.

model-by-model analyses are therefore necessary to diagnose both the nature of the forced responses in the CMIP6 models and the dynamics of internal variability that drive the simulated trends.

4. Conclusions

We have tested several large collections of model simulations for their ability to simulate the observed twentieth-to-twenty-first-century precipitation trend over SESA. There is an ongoing discussion as to what drives the observed wetting trend and on which time scales. On interannual time scales, SESA precipitation is driven by ENSO and SAM (e.g., [Silvestri and Vera 2003](#); [Seager et al. 2010](#)). On multidecadal time scales, tropical Atlantic variability has driven much of the trend ([Seager et al. 2010](#)). Since 1960, a poleward shift in the descending branch of the Hadley cell as a result of stratospheric ozone depletion also contributed to the trend ([Gonzalez et al. 2014](#)). Stratospheric ozone depletion is thought to have caused a precipitation increase that is at least as large as the increase caused by GHG forcing alone ([Gonzalez et al. 2014](#); [Zhang et al. 2016](#)). As emissions of ozone-depleting substances are reduced and ozone recovers, the wetting response associated with the ozone depletion is likely to plateau or reverse, even as GHG emissions continue to march upward. It is unclear how hydroclimate in SESA will

respond to these opposing forcings without a better understanding of how much they have contributed to observed trends to date.

The two SST-forced simulations, which should include the SESA variability driven by the tropical Pacific and Atlantic plus the anthropogenic imprint on SSTs, simulate a forced response that is positive but less than 25% of the observed trend. The cause of the amplitude discrepancy between the observed precipitation trend and the SST-forced precipitation trend is likely a result of one or a combination of the following: 1) the SESA trend forced by SSTs in the models is too weak, 2) internal atmospheric variability is too weak, or 3) important atmospheric trends forced by anthropogenic emissions are not reflected in the SST-forced runs (e.g., ozone depletion). Explanations 1 and 2 could both be a result of the lack of atmosphere–ocean coupling in the SST-forced experiments and/or poor atmospheric teleconnections simulated in these two models.

The CMIP models contain both atmosphere–ocean coupling and all radiative forcings. While CMIP5 simulates a trend comparable to the SST-forced simulations, the most recent, state-of-the-art CMIP6-based estimates of precipitation trends are weaker. As GHG forcing increases through CMIP6 SSP5-8.5, the models tend to simulate an increase in precipitation; however, the multimodel median trend is always weaker than the observed twentieth-to-twenty-first-century trend.

We also find that the observed trend falls at the tail end of the distribution simulated in long preindustrial control runs. Some model simulations do include a rare 85-yr trend that crosses the lower range of the twentieth-to-twenty-first-century trends estimated from observations, but most models do not appear capable of producing a trend as large as that observed due to internal variability alone. Given expectations that the observed trend is a combination of anthropogenic forcing and internal variability, we might not expect the historical simulations or the preindustrial control runs to alone simulate the trend. That is, the historical simulations, particularly the single-run or small-ensemble simulations, only sample one or a few realizations of internal variability, while the preindustrial control simulations do not contain the effects of anthropogenic forcing. However, the near absence of simulated trends within the many model simulations we evaluated for the historical, preindustrial, and SST-forced scenarios that are as strong as those in the observations suggests the models systematically exhibit a forced response that is too weak and/or internal variability that is also underestimated.

The findings presented herein corroborate and highlight some of the previous literature that established the influence of SST variability on SESA precipitation variability and precipitation increases (e.g., Seager et al. 2010) and the anthropogenic influence on SESA precipitation (e.g., Gonzalez et al. 2014; Zhang et al. 2016). Our findings support suggestions that internal variability is underestimated in current state-of-the-art models and the forced response may also be too small. Further work is needed to gain a better understanding of what is driving precipitation variability and trends in observations and individual model simulations. An improved understanding of the relative contributions of SSTs versus anthropogenic trends, as well as their combined influence on SESA precipitation trends over the twentieth to twenty-first centuries, is needed, in addition to model-by-model analyses of how and why the largest positive precipitation trends over SESA are simulated. Assessing the impacts of horizontal resolution on simulated trends is something that we have not explored in this study, but it could be important for understanding the modeled trend discrepancies. Initial assessments (not shown) suggest the influence of model resolution on simulated SESA precipitation trends is limited but more work is left to be done on this topic.

Taking our current results at face value, a critical question arises: how should the projected precipitation trends over SESA be interpreted? If the model forced trend is too weak, then the real-world SESA could become even wetter than current models project. On the other hand, if modeled internal variability is too weak, future internal variability in the real-world could add to the forced response or counteract it, perhaps even driving a return to a drier climate in SESA. The situation is even more confused, however, because the relative importance of ozone and GHG forcing for SESA precipitation is unclear, leaving the combined influence of one reducing and one increasing influence hard to parse in the future. The bottom line is that—at present and given the ambiguous trends in SESA precipitation over the twentieth to twenty-first centuries in the SST-forced, fully coupled, and preindustrial control simulations—many futures for SESA can be imagined. This

result needs to be reflected in a risk analysis of precipitation in SESA that more accurately represents the range of possible outcomes beyond the ensemble mean and spread of CMIP5 and CMIP6 projections. Fundamentally, a greatly improved dynamical understanding of the drivers of long-term precipitation changes in SESA is needed before confidence can be placed in the projections of precipitation over this critical region.

Acknowledgments. This research was supported by the National Science Foundation Partnerships for International Research and Education Award OISE-1743738 and the National Science Foundation Grant AGS-1602581. We thank Naomi Henderson and Dong-Eun Lee for the NCAR SST-forced simulations used in this paper, and we thank Naomi Henderson and Haibo Liu for assistance with the CMIP5 data. We also thank the National Science Foundation Award 1760648 for CMIP6 data accessed through Google Cloud.

Data availability statement. CMIP data are available from the Earth System Grid and Lawrence Livermore National Laboratory (<https://esgf-node.llnl.gov/projects/esgf-llnl/>). The SST-forced simulations are available from the Lamont-Doherty Earth Observatory Ocean and Climate Physics Data Library (<http://dolphy.ldeo.columbia.edu:81/SOURCES/DTF/LDEO/>). Observed precipitation data are from the University of East Anglia Climatic Research Unit (<https://catalogue.ceda.ac.uk/uuid/89e1e34ec3554dc98594a5732622bce9>) as cited in Harris et al. (2020), and GPCC Full Data Monthly Product Version 2018 can be accessed at https://doi.org/10.5676/DWD_GPCC/FD_M_V2018_050.

REFERENCES

- Andreoli, R. V., and M. T. Kayano, 2005: ENSO-related rainfall anomalies in South America and associated circulation features during warm and cold Pacific decadal oscillation regimes. *Int. J. Climatol.*, **25**, 2017–2030, <https://doi.org/10.1002/joc.1222>.
- Arblaster, J. M., G. A. Meehl, and D. J. Karoly, 2011: Future climate change in the Southern Hemisphere: Competing effects of ozone and greenhouse gases. *Geophys. Res. Lett.*, **38**, L02701, <https://doi.org/10.1029/2010GL045384>.
- Baldi, G., and J. M. Paruelo, 2008: Land-use and land cover dynamics in South American temperate grasslands. *Ecol. Soc.*, **13**, 6, <https://doi.org/10.5751/ES-02481-130206>.
- Barreiro, M., N. Díaz, and M. Renom, 2014: Role of the global oceans and land-atmosphere interaction on summertime interdecadal variability over northern Argentina. *Climate Dyn.*, **42**, 1733–1753, <https://doi.org/10.1007/s00382-014-2088-6>.
- Barros, V. R., M. E. Doyle, and I. A. Camilloni, 2008: Precipitation trends in southeastern South America: Relationship with ENSO phases and with low-level circulation. *Theor. Appl. Climatol.*, **93**, 19–33, <https://doi.org/10.1007/s00704-007-0329-x>.
- Bonfils, C., and B. D. Santer, 2011: Investigating the possibility of a human component in various Pacific decadal oscillation indices. *Climate Dyn.*, **37**, 1457–1468, <https://doi.org/10.1007/s00382-010-0920-1>.
- Carvalho, L. M. V., 2020: Assessing precipitation trends in the Americas with historical data: A review. *Wiley Interdiscip. Rev.: Climate Change*, **11**, e627, <https://doi.org/10.1002/wcc.627>.

- Cazes-Boezio, G., A. W. Robertson, and C. R. Mechoso, 2003: Seasonal dependence of ENSO teleconnections over South America and relationships with precipitation in Uruguay. *J. Climate*, **16**, 1159–1176, [https://doi.org/10.1175/1520-0442\(2003\)16<1159:SDOETO>2.0.CO;2](https://doi.org/10.1175/1520-0442(2003)16<1159:SDOETO>2.0.CO;2).
- Chilukoti, N., and Y. Xue, 2021: An assessment of potential climate impact during 1948–2010 using historical land use land cover change maps. *Int. J. Climatol.*, **41**, 295–315, <https://doi.org/10.1002/joc.6621>.
- Cook, B. I., J. S. Mankin, K. Marvel, A. P. Williams, J. E. Smerdon, and K. J. Anchukaitis, 2020: Twenty-first century drought projections in the CMIP6 forcing scenarios. *Earth's Future*, **8**, e2019EF001461, <https://doi.org/10.1029/2019EF001461>.
- Dai, A., 2021: Hydroclimatic trends during 1950–2018 over global land. *Climate Dyn.*, **56**, 4027–4049, <https://doi.org/10.1007/s00382-021-05684-1>.
- Dätwyler, C., M. Grosjean, N. J. Steiger, and R. Neukom, 2020: Teleconnections and relationship between the El Niño–Southern Oscillation (ENSO) and the southern annular mode (SAM) in reconstructions and models over the past millennium. *Climate Past*, **16**, 743–756, <https://doi.org/10.5194/cp-16-743-2020>.
- de Barros Soares, D., H. Lee, P. C. Loikith, A. Barkhordarian, and C. R. Mechoso, 2017: Can significant trends be detected in surface air temperature and precipitation over South America in recent decades? *Int. J. Climatol.*, **37**, 1483–1493, <https://doi.org/10.1002/joc.4792>.
- Deser, C., A. S. Phillips, and J. W. Hurrell, 2004: Pacific interdecadal climate variability: Linkages between the tropics and the North Pacific during boreal winter since 1900. *J. Climate*, **17**, 3109–3124, [https://doi.org/10.1175/1520-0442\(2004\)017<3109:PICVLB>2.0.CO;2](https://doi.org/10.1175/1520-0442(2004)017<3109:PICVLB>2.0.CO;2).
- Díaz, L. B., and C. S. Vera, 2017: Austral summer precipitation interannual variability and trends over southeastern South America in CMIP5 models. *Int. J. Climatol.*, **37**, 681–695, <https://doi.org/10.1002/joc.5031>.
- , R. I. Saurral, and C. S. Vera, 2021: Assessment of South America summer rainfall climatology and trends in a set of global climate models large ensembles. *Int. J. Climatol.*, **41**, E59–E77, <https://doi.org/10.1002/joc.6643>.
- Enfield, D. B., A. M. Mestas-Núñez, and P. J. Trimble, 2001: The Atlantic multidecadal oscillation and its relation to rainfall and river flows in the continental U.S. *Geophys. Res. Lett.*, **28**, 2077–2080, <https://doi.org/10.1029/2000GL012745>.
- Eyring, V., S. Bony, G. A. Meehl, C. A. Senior, B. Stevens, R. J. Stouffer, and K. E. Taylor, 2016: Overview of the Coupled Model Intercomparison Project phase 6 (CMIP6) experimental design and organization. *Geosci. Model Dev.*, **9**, 1937–1958, <https://doi.org/10.5194/gmd-9-1937-2016>.
- Folland, C. K., D. E. Parker, A. W. Colman, and R. Washington, 1999: Large scale modes of ocean surface temperature since the late nineteenth century. *Beyond El Niño: Decadal and Interdecadal Climate Variability*, A. Navarra, Ed., Springer, 73–102.
- Genta, J., G. Perez-Iribarren, and C. R. Mechoso, 1998: A recent increasing trend in the streamflow of rivers in southeastern South America. *J. Climate*, **11**, 2858–2862, [https://doi.org/10.1175/1520-0442\(1998\)011<2858:ARITIT>2.0.CO;2](https://doi.org/10.1175/1520-0442(1998)011<2858:ARITIT>2.0.CO;2).
- Gillett, N. P., and D. W. J. Thompson, 2003: Simulation of recent Southern Hemisphere climate change. *Science*, **302**, 273–275, <https://doi.org/10.1126/science.1087440>.
- Gonzalez, P. L. M., L. M. Polvani, R. Seager, and G. J. P. Correa, 2014: Stratospheric ozone depletion: A key driver of recent precipitation trends in South Eastern South America. *Climate Dyn.*, **42**, 1775–1792, <https://doi.org/10.1007/s00382-013-1777-x>.
- Grimm, A. M., V. R. Barros, and M. E. Doyle, 2000: Climate variability in Southern South America associated with El Niño and La Niña events. *J. Climate*, **13**, 35–58, [https://doi.org/10.1175/1520-0442\(2000\)013<0035:CVISSA>2.0.CO;2](https://doi.org/10.1175/1520-0442(2000)013<0035:CVISSA>2.0.CO;2).
- Grothe, P. R., and Coauthors, 2020: Enhanced El Niño–Southern Oscillation variability in recent decades. *Geophys. Res. Lett.*, **47**, e2019GL083906, <https://doi.org/10.1029/2019GL083906>.
- Hamed, K. H., 2008: Trend detection in hydrologic data: The Mann–Kendall trend test under the scaling hypothesis. *J. Hydrol.*, **349**, 350–363, <https://doi.org/10.1016/j.jhydrol.2007.11.009>.
- Harris, I., T. J. Osborn, P. Jones, and D. Lister, 2020: Version 4 of the CRU TS monthly high-resolution gridded multivariate climate dataset. *Sci. Data*, **7**, 109, <https://doi.org/10.1038/s41597-020-0453-3>.
- Haylock, M. R., and Coauthors, 2006: Trends in total and extreme South American rainfall in 1960–2000 and links with sea surface temperature. *J. Climate*, **19**, 1490–1512, <https://doi.org/10.1175/JCLI3695.1>.
- Kaplan, A., M. A. Cane, Y. Kushnir, A. C. Clement, M. B. Blumenthal, and B. Rajagopalan, 1998: Analyses of global sea surface temperature 1856–1991. *J. Geophys. Res. Oceans*, **103**, 18 567–18 589, <https://doi.org/10.1029/97JC01736>.
- Kay, J. E., and Coauthors, 2015: The Community Earth System Model (CESM) large ensemble project: A community resource for studying climate change in the presence of internal climate variability. *Bull. Amer. Meteor. Soc.*, **96**, 1333–1349, <https://doi.org/10.1175/BAMS-D-13-00255.1>.
- Kayano, M. T., and R. V. Andreoli, 2007: Relations of South American summer rainfall interannual variations with the Pacific decadal oscillation. *Int. J. Climatol.*, **27**, 531–540, <https://doi.org/10.1002/joc.1417>.
- , —, and R. A. F. de Souza, 2020: Pacific and Atlantic multidecadal variability relations to the El Niño events and their effects on the South American rainfall. *Int. J. Climatol.*, **40**, 2183–2200, <https://doi.org/10.1002/joc.6326>.
- Kerr, R. A., 2000: A North Atlantic climate pacemaker for the centuries. *Science*, **288**, 1984–1985, <https://doi.org/10.1126/science.288.5473.1984>.
- Kiehl, J., J. Hack, G. Bonan, B. Boville, D. Williamson, and P. Rasch, 1998: The National Center for Atmospheric Research Community Climate Model: CCM3. *J. Climate*, **11**, 1131–1149, [https://doi.org/10.1175/1520-0442\(1998\)011<1131:TNCFA>2.0.CO;2](https://doi.org/10.1175/1520-0442(1998)011<1131:TNCFA>2.0.CO;2).
- Lee, J.-E., B. R. Lintner, C. K. Boyce, and P. J. Lawrence, 2011: Land use change exacerbates tropical South American drought by sea surface temperature variability. *Geophys. Res. Lett.*, **38**, L19706, <https://doi.org/10.1029/2011GL049066>.
- L'Heureux, M. L., and D. W. J. Thompson, 2006: Observed relationships between the El Niño–Southern Oscillation and the extratropical zonal-mean circulation. *J. Climate*, **19**, 276–287, <https://doi.org/10.1175/JCLI3617.1>.
- Li, J., and Coauthors, 2011: Interdecadal modulation of El Niño amplitude during the past millennium. *Nat. Climate Change*, **1**, 114–118, <https://doi.org/10.1038/nclimate1086>.
- Liebmann, B., and Coauthors, 2004: An observed trend in central South American precipitation. *J. Climate*, **17**, 4357–4367, <https://doi.org/10.1175/3205.1>.
- Lucas, C., P. Puchi, L. Profumo, A. Ferreira, and A. Muñoz, 2018: Effect of climate on tree growth in the Pampa biome of southeastern South America: First tree-ring chronologies from Uruguay. *Dendrochronologia*, **52**, 113–122, <https://doi.org/10.1016/j.dendro.2018.10.004>.

- Magrin, G. O., M. I. Travasso, and G. R. Rodríguez, 2005: Changes in climate and crop production during the 20th century in Argentina. *Climatic Change*, **72**, 229–249, <https://doi.org/10.1007/s10584-005-5374-9>.
- Mantua, N. J., and S. R. Hare, 2002: The Pacific decadal oscillation. *J. Oceanogr.*, **58**, 35–44, <https://doi.org/10.1023/A:1015820616384>.
- , —, Y. Zhang, J. M. Wallace, and R. C. Francis, 1997: A Pacific interdecadal climate oscillation with impacts on salmon production. *Bull. Amer. Meteor. Soc.*, **78**, 1069–1080, [https://doi.org/10.1175/1520-0477\(1997\)078<1069:APICOW>2.0.CO;2](https://doi.org/10.1175/1520-0477(1997)078<1069:APICOW>2.0.CO;2).
- Marshall, G. J., 2003: Trends in the southern annular mode from observations and reanalyses. *J. Climate*, **16**, 4134–4143, [https://doi.org/10.1175/1520-0442\(2003\)016<4134:TITSAM>2.0.CO;2](https://doi.org/10.1175/1520-0442(2003)016<4134:TITSAM>2.0.CO;2).
- McGregor, S., A. Timmermann, M. England, O. Timm, and A. Wittenberg, 2013: Inferred changes in El Niño–Southern Oscillation variance over the past six centuries. *Climate Past*, **9**, 2269–2284, <https://doi.org/10.5194/cp-9-2269-2013>.
- McLandress, C., T. G. Shepherd, J. F. Scinocca, D. A. Plummer, M. Sigmond, A. I. Jonsson, and M. C. Reader, 2011: Separating the dynamical effects of climate change and ozone depletion. Part II: Southern Hemisphere troposphere. *J. Climate*, **24**, 1850–1868, <https://doi.org/10.1175/2010JCLI3958.1>.
- Neale, R. B., and Coauthors, 2010: Description of the NCAR Community Atmosphere Model (CAM 5.0). NCAR Tech. Note NCAR/TN-486+ STR, 268 pp., www.cesm.ucar.edu/models/cesm1.1/cam/docs/description/cam5_desc.pdf.
- O'Neill, B. C., and Coauthors, 2017: The roads ahead: Narratives for shared socioeconomic pathways describing world futures in the 21st century. *Global Environ. Change*, **42**, 169–180, <https://doi.org/10.1016/j.gloenvcha.2015.01.004>.
- Perlwitz, J., S. Pawson, R. L. Fogt, J. E. Nielsen, and W. D. Neff, 2008: Impact of stratospheric ozone hole recovery on Antarctic climate. *Geophys. Res. Lett.*, **35**, L08714, <https://doi.org/10.1029/2008GL033317>.
- Pisciottano, G., A. Díaz, G. Cazess, and C. R. Mechoso, 1994: El Niño–Southern Oscillation impact on rainfall in Uruguay. *J. Climate*, **7**, 1286–1302, [https://doi.org/10.1175/1520-0442\(1994\)007<1286:ENSOIO>2.0.CO;2](https://doi.org/10.1175/1520-0442(1994)007<1286:ENSOIO>2.0.CO;2).
- Polvani, L. M., D. W. Waugh, G. J. P. Correa, and S.-W. Son, 2011: Stratospheric ozone depletion: The main driver of twentieth-century atmospheric circulation changes in the Southern Hemisphere. *J. Climate*, **24**, 795–812, <https://doi.org/10.1175/2010JCLI3772.1>.
- Power, S., T. Casey, C. Folland, A. Colman, and V. Mehta, 1999: Interdecadal modulation of the impact of ENSO on Australia. *Climate Dyn.*, **15**, 319–324, <https://doi.org/10.1007/s003820050284>.
- Robertson, A. W., and C. R. Mechoso, 1998: Interannual and decadal cycles in river flows of southeastern South America. *J. Climate*, **11**, 2570–2581, [https://doi.org/10.1175/1520-0442\(1998\)011<2570:IADCIR>2.0.CO;2](https://doi.org/10.1175/1520-0442(1998)011<2570:IADCIR>2.0.CO;2).
- Rudolf, B., A. Becker, U. Schneider, A. Meyer-Christoffer, and M. Ziese, 2010: The new “GPCC Full Data Reanalysis Version 5” providing high-quality gridded monthly precipitation data for the global land-surface is public available since December 2010. GPCC Status Rep., 7 pp., https://www.dwd.de/EN/ourservices/gpcc/reports_publications/GPCC_status_report_2010.pdf?__blob=publicationFile&v=3.
- Salazar, A., G. Baldi, M. Hirota, J. Syktus, and C. McAlpine, 2015: Land use and land cover change impacts on the regional climate of non-Amazonian South America: A review. *Global Planet. Change*, **128**, 103–119, <https://doi.org/10.1016/j.gloplacha.2015.02.009>.
- Schlesinger, M. E., and N. Ramankutty, 1994: An oscillation in the global climate system of period 65–70 years. *Nature*, **367**, 723–726, <https://doi.org/10.1038/367723a0>.
- Schnepf, R. D., E. N. Dohlmán, and H. C. Bolling, 2001: Agriculture in Brazil and Argentina: Developments and prospects for major field crops. U.S. Department of Agriculture Doc., 85 pp., <https://www.ers.usda.gov/publications/pub-details/?pubid=40353>.
- Seager, R., Y. Kushnir, C. Herweijer, N. Naik, and J. Velez, 2005: Modeling of tropical forcing of persistent droughts and pluvials over western North America: 1856–2000. *J. Climate*, **18**, 4065–4088, <https://doi.org/10.1175/JCLI3522.1>.
- , N. Naik, W. Baethgen, A. Robertson, Y. Kushnir, J. Nakamura, and S. Jurburg, 2010: Tropical oceanic causes of interannual to multidecadal precipitation variability in Southeast South America over the past century. *J. Climate*, **23**, 5517–5539, <https://doi.org/10.1175/2010JCLI3578.1>.
- Silvestri, G. E., and C. S. Vera, 2003: Antarctic oscillation signal on precipitation anomalies over southeastern South America. *Geophys. Res. Lett.*, **30**, 2115, <https://doi.org/10.1029/2003GL018277>.
- Son, S.-W., and Coauthors, 2008: The impact of stratospheric ozone recovery on the Southern Hemisphere westerly jet. *Science*, **320**, 1486–1489, <https://doi.org/10.1126/science.1155939>.
- , N. F. Tandon, L. M. Polvani, and D. W. Waugh, 2009: Ozone hole and Southern Hemisphere climate change. *Geophys. Res. Lett.*, **36**, L15705, <https://doi.org/10.1029/2009GL038671>.
- , and Coauthors, 2010: Impact of stratospheric ozone on Southern Hemisphere circulation change: A multimodel assessment. *J. Geophys. Res.*, **115**, D00M07, <https://doi.org/10.1029/2010JD014271>.
- Taylor, K. E., R. J. Stouffer, and G. A. Meehl, 2012: An overview of CMIP5 and the experiment design. *Bull. Amer. Meteor. Soc.*, **93**, 485–498, <https://doi.org/10.1175/BAMS-D-11-00094.1>.
- Thompson, D. W. J., and S. Solomon, 2002: Interpretation of recent Southern Hemisphere climate change. *Science*, **296**, 895–899, <https://doi.org/10.1126/science.1069270>.
- , J. M. Wallace, and G. C. Hegerl, 2000: Annular modes in the extratropical circulation. Part II: Trends. *J. Climate*, **13**, 1018–1036, [https://doi.org/10.1175/1520-0442\(2000\)013<1018:AMITEC>2.0.CO;2](https://doi.org/10.1175/1520-0442(2000)013<1018:AMITEC>2.0.CO;2).
- , S. Solomon, P. J. Kushner, M. H. England, K. M. Grise, and D. J. Karoly, 2011: Signatures of the Antarctic ozone hole in Southern Hemisphere surface climate change. *Nat. Geosci.*, **4**, 741–749, <https://doi.org/10.1038/ngeo1296>.
- Tindall, J. C., A. M. Haywood, and F. W. Howell, 2016: Accounting for centennial-scale variability when detecting changes in ENSO: A study of the Pliocene. *Paleoceanography*, **31**, 1330–1349, <https://doi.org/10.1002/2016PA002951>.
- Ting, M., Y. Kushnir, R. Seager, and C. Li, 2009: Forced and internal twentieth-century SST trends in the North Atlantic. *J. Climate*, **22**, 1469–1481, <https://doi.org/10.1175/2008JCLI2561.1>.
- Vera, C. S., and L. Díaz, 2015: Anthropogenic influence on summer precipitation trends over South America in CMIP5 models. *Int. J. Climatol.*, **35**, 3172–3177, <https://doi.org/10.1002/joc.4153>.
- Viglizzo, E. F., and F. C. Frank, 2006: Ecological interactions, feedbacks, thresholds and collapses in the Argentine Pampas in response to climate and farming during the last century. *Quat. Int.*, **158**, 122–126, <https://doi.org/10.1016/j.quaint.2006.05.022>.
- Xue, Y., F. de Sales, W.-P. Li, C. R. Mechoso, C. A. Nobre, and H.-M. Juang, 2006: Role of land surface processes in South American monsoon development. *J. Climate*, **19**, 741–762, <https://doi.org/10.1175/JCLI3667.1>.

- Zhang, H., T. L. Delworth, F. Zeng, G. Vecchi, K. Paffendorf, and L. Jia, 2016: Detection, attribution, and projection of regional rainfall changes on (multi-) decadal time scales: A focus on southeastern South America. *J. Climate*, **29**, 8515–8534, <https://doi.org/10.1175/JCLI-D-16-0287.1>.
- Zhang, Y., J. M. Wallace, and D. S. Battisti, 1997: ENSO-like interdecadal variability: 1900–93. *J. Climate*, **10**, 1004–1020, [https://doi.org/10.1175/1520-0442\(1997\)010<1004:ELIV>2.0.CO;2](https://doi.org/10.1175/1520-0442(1997)010<1004:ELIV>2.0.CO;2).
- Zilli, M. T., L. M. V. Carvalho, B. Liebmann, and M. A. Silva Dias, 2017: A comprehensive analysis of trends in extreme precipitation over southeastern coast of Brazil. *Int. J. Climatol.*, **37**, 2269–2279, <https://doi.org/10.1002/joc.4840>.
- Zortea, R. B., V. G. Maciel, and A. Passuello, 2018: Sustainability assessment of soybean production in southern Brazil: A life cycle approach. *Sustain. Prod. Consump.*, **13**, 102–112, <https://doi.org/10.1016/j.spc.2017.11.002>.